Supplementary Information

Self-assembled air-stable magnesium hydride embedded in 3-D activated carbon for reversible hydrogen storage

*S.S. Shinde, Dong-Hyung Kim, Jin-Young Yu, Jung-Ho Lee**

Department of Materials and Chemical Engineering, Hanyang University, Ansan, Kyunggido, 426-791, Republic of Korea

Email: jungho@hanyang.ac.kr

Experimental methods

Detailed NMR resonances

We utilized a magic-sandwich-echo pulse sequence led by two 90° pulses with flashing same and opposite phases to attain factual line shapes.[S1]

$$90^0_{+x} - 90^0_{\pm x} - T - 90^0_{\phi} - \tau - 90^0_{\psi} - \left(\tau_{MSE} - 90^0_{\phi} - \tau_{MSE}\right)_4 \left(\tau_{MSE} - 90^0_{-\phi} - \tau_{MSE}\right)_4 - 90^0_{\psi} - \tau - \det ection_{\pm\phi} \quad (1)$$

Where, the pulse phases φ and ψ are connected by 90° phase shift, ψ = φ +90°. The 90° pulse duration was 2 μs. The intervals of pulse for τ_{MSE} and τ were 2 and 8 μs. The pre-detection delay of τ was 5.5 μs.

Adjusting proper cycles of φ and ψ phases, the initial $90^0_{+x} - 90^0_{\pm x}$ pulse pair effectively prevents the accumulation of echo's and ensures baseline. For quantitative purpose the (z-filter) time T following the initial two pulses was taken 10 ms, which is large compared to proton transversal relaxation T_2, but negligibly short with respect to the spin-lattice relaxation T_1. T_1–weighed spectra were recorded with T = 1s, and T_1 relaxation was measured by varying T. The subsequent NMR relaxation delay scans was taken 900 s for the hybrids and 3600 s for bulk MgH_2.

Results and discussion

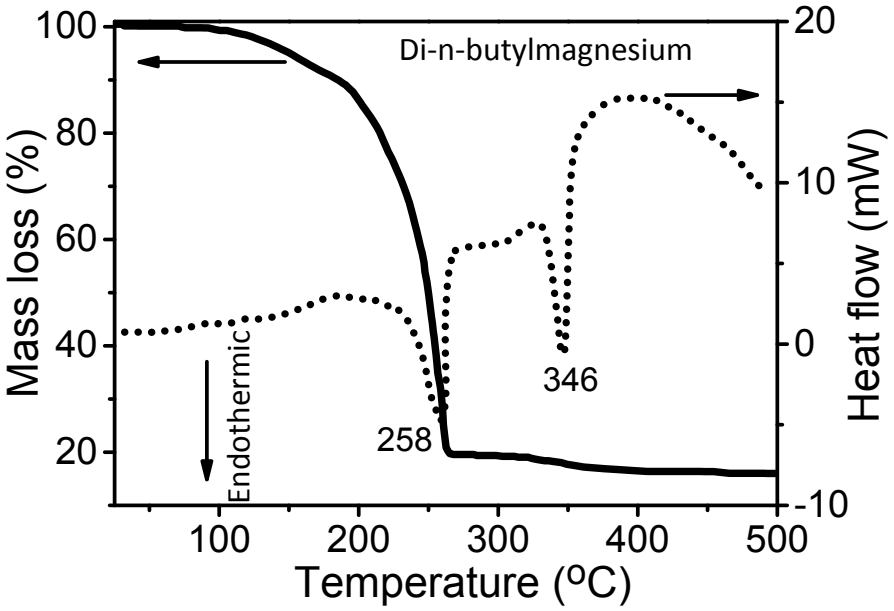

Figure S1. Thermogravimetric analysis (TGA) and differential scanning calorimetry (DSC) profiles of Di-n-butylmagnesium (solid and dashed lines, respectively).

The TGA results show that the majority of the organic motif (Di-n-butylmagnesium) decomposes steeply from 100 °C with a loss of mass ~ 80.65 up to 265 °C. Further, the observed endothermic weight loss peak at 258 °C corresponds to complete decomposition of the butyl group in terms of 1-butene and associated fragments. Besides, the release of residual butyl, the observed endothermic peak at 346 °C confirms the significant evolution of hydrogen with 3.27 % mass loss respect to rising temperatures.[S2]

The overall decomposition follows two steps as per following reactions in the range of 100-265 °C (equation 1) and 265-400 °C (equation 2).[S2]

$$(C_4H_9)_2Mg \rightarrow (2-x)C_4H_{8(g)} + x(C_4H_8)_{surf}MgH_{2(s)} \quad (1)$$

$$(C_4H_8)_{surf}MgH_{2(s)} \rightarrow C_4H_{8(g)} + MgH_{2(s)} \rightarrow Mg_{(s)} + H_{2(g)} \quad (2)$$

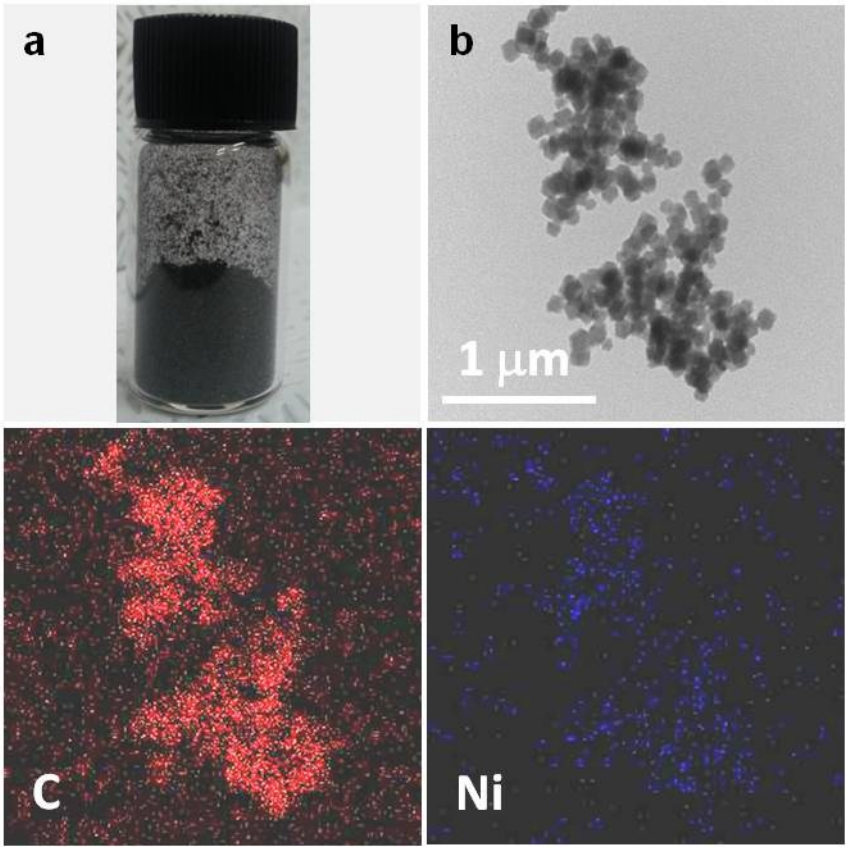

Figure S2. (a) Photograph and (b) STEM image of metal-interacted three-dimensional carbon and the corresponding elemental mappings of C, and Ni. The corresponding elemental mapping analysis confirms the well-dispersed Ni coordination with C. The observed percentage of Ni was 3.2 at%.

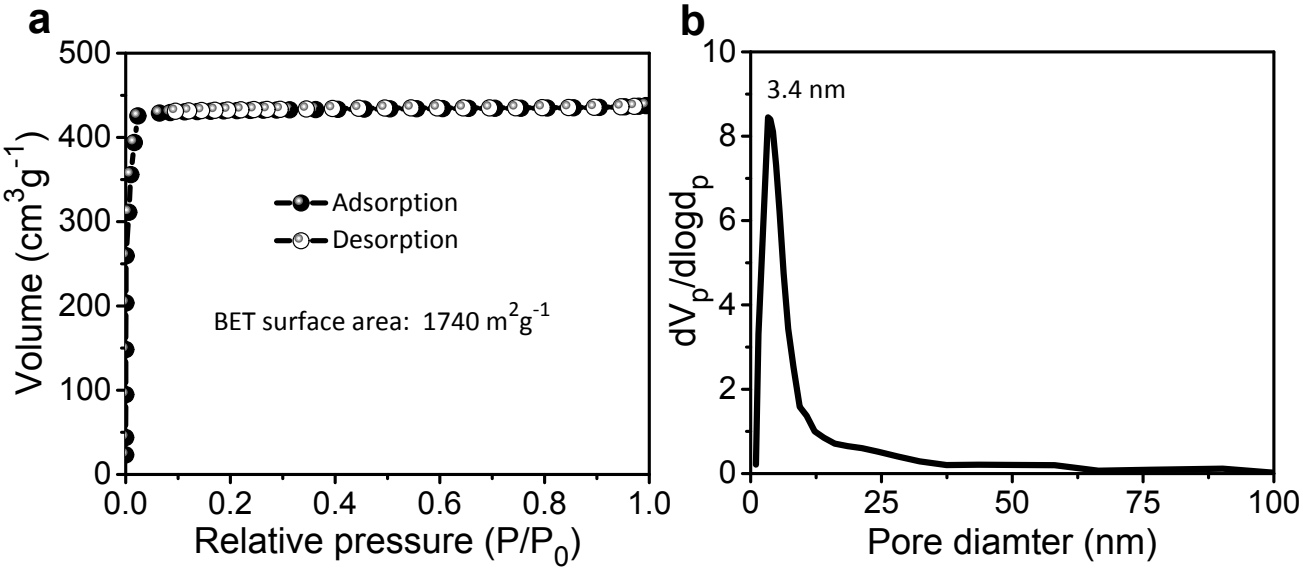

Figure S3. (a) N_2 adsorption−desorption isotherms and (b) pore size distributions of the prepared 3-D carbon structures.

The N_2 sorption isotherms exhibit an important characteristic of a type-I pattern (typical H_2 hysteresis loop) with an abrupt climb at a relatively low pressure ($P/P_0 < 0.1$), confirming the presence of micropores and mesopores. Further, the pore distribution plot shows a sharp peak at 3.4 nm. Overall, the present data confirms the developed flexible 3-D carbon with a mesoporous structure has a large surface area, appropriate pore size, and high pore volume is an adequate host for bifunctional applications such as the conversion and storage of hydrogen.

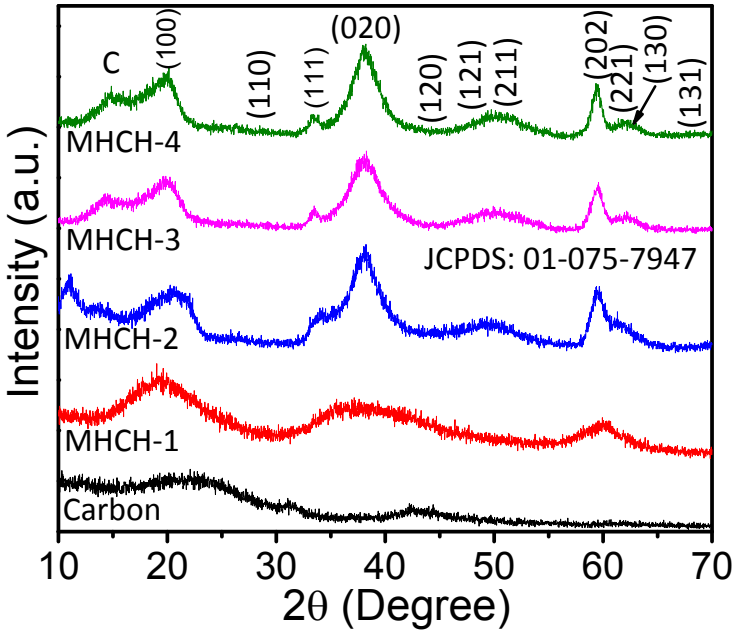

Figure S4. X-ray diffraction patterns of carbon and the MHCH-1, MHCH-2, MHCH-3, and MHCH-4 samples.

The XRD pattern of MHCH-1 shows broad peaks of amorphous carbon and magnesium, confirming that the triethanolamine cannot support the hydrogenation reaction. Further, the formation of MgH_2 in the remaining MHCH catalysts after the solvothermal reaction without any impurity phases was confirmed in the presence of hydrazine hydrate. Surprisingly, despite of the reactions (e.g., MHCH-1 and MHCH-2), the presence of transition metal cations[S3] with carbon architectures drastically enhances the hydrogen selectivity (e.g. MHCH-3, MHCH-4, and MHCH-5), demonstrating that hydrous hydrazine can be completely converted to hydrogen at room temperature. This confirms the development of cost-effective, high performing, and environmentally benign catalysts as a promising hydrogen storage material which may encourage the effective application of hydrous hydrazine during the solvothermal reaction at room temperature.

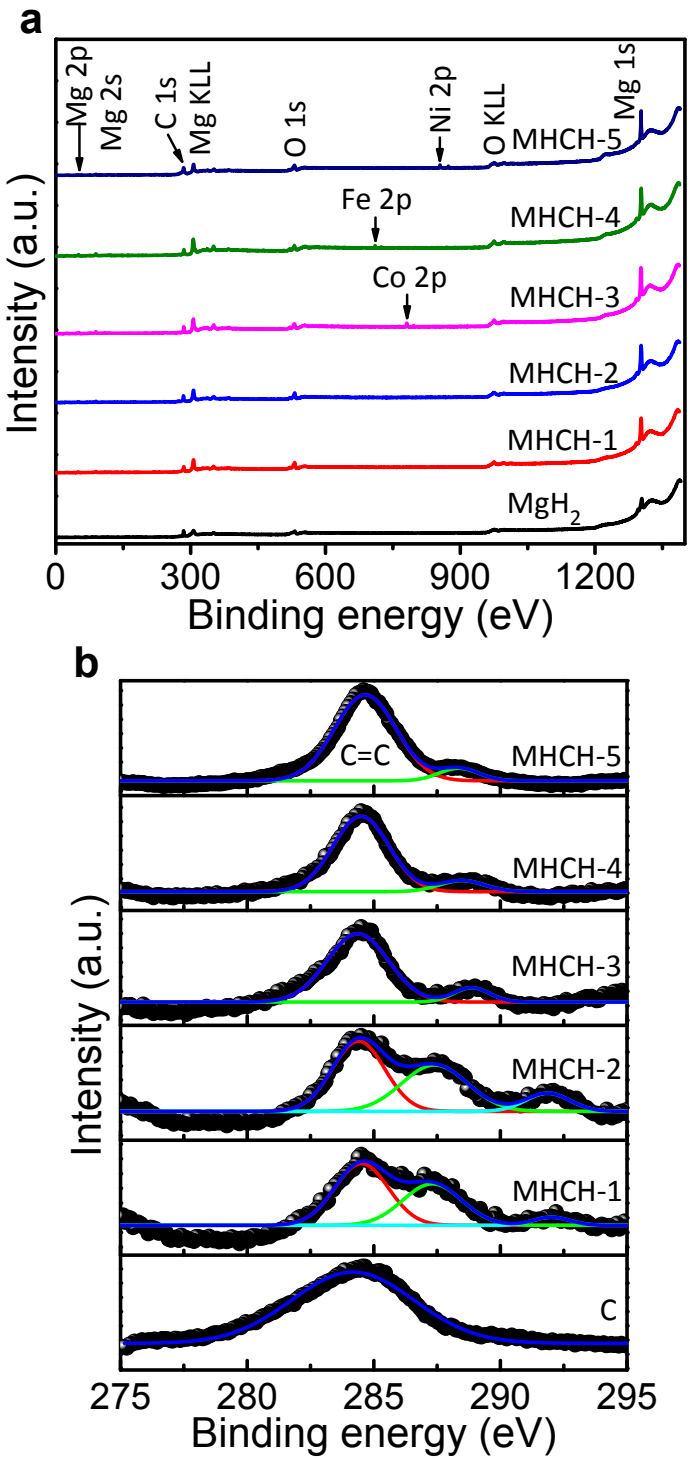

Figure S5. (a) XPS survey scan spectra of bulk MgH_2 and prepared MHCH samples. (b) Curve-fit high-resolution XPS spectra of C 1s for C, and the prepared MHCH samples.

The C 1s spectra exhibit the largest graphitic carbon signal at 284.7 eV (sp^2 C=C) and a minor signal at 288.5 eV (C-H functional group).[S4] Moreover, the additional peak at 292 eV was observed for MHCH-1 and MHCH-2 samples, however it is absent in MHCH-3, MHCH-4 and MHCH-5 samples.

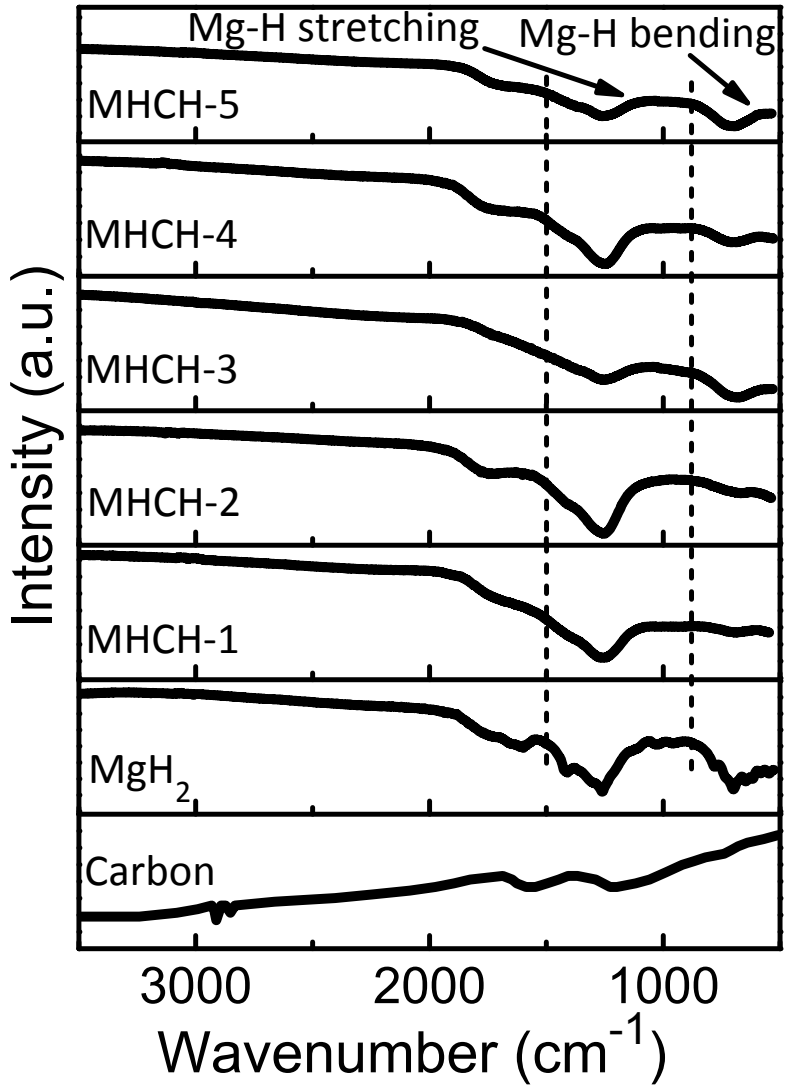

Figure S6. Fourier transform infrared (FTIR) spectra of carbon, bulk MgH_2, and as-synthesized MHCH samples.

The FTIR spectra of the prepared MHCH samples compared to pristine carbon indicate the successful formation of the MgH_2 phase. The FTIR spectra of MHCH samples display two main regions of active infrared vibrations of the Mg-H bonds in the ranges of 500-800 and 800-1,500 cm^{-1}, which are assigned to the Mg-H bending bands and the Mg–H stretching bands, respectively.[S5, S6] In the present case, the bending and stretching vibrations of the as-synthesized MHCH samples are centered at ~ 706.2 and 1,256.8 cm^{-1}, respectively. Further, transition metal containing phases were not detected because of their lower concentrations and the in-built 3-D architecture of carbon.

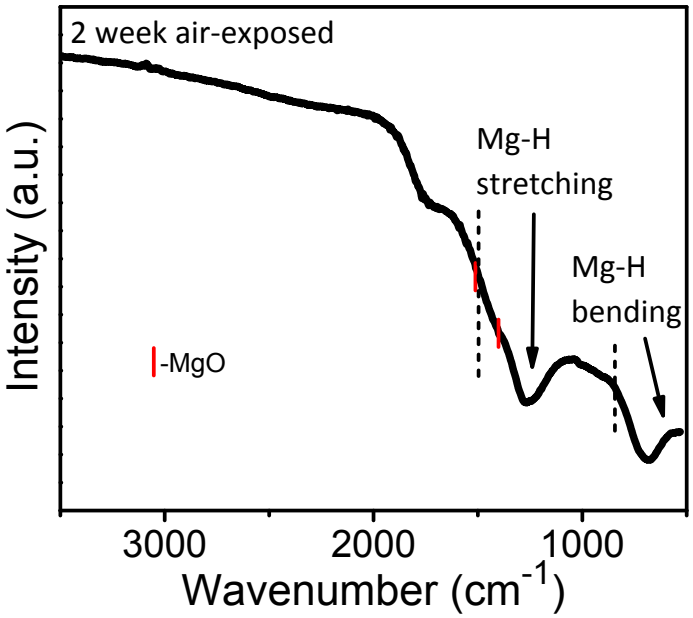

Figure S7. FTIR spectrum of the MHCH-5 exposed to air for two weeks.

We did not observe any detectable percentage for oxidation with our MHCH-5 with air exposing for 2 weeks. Therefore, the weak signals of MgO are not clearly seen in figure above. However, if we see carefully, extremely weak shoulders are seen at 1410 and 1506 cm^{-1}, which may be because of oxide content.[S7] Further, this FTIR results are well agreed with XRD patterns confirming there is no any change in crystalline structure in as-prepared and air-exposed catalysts.

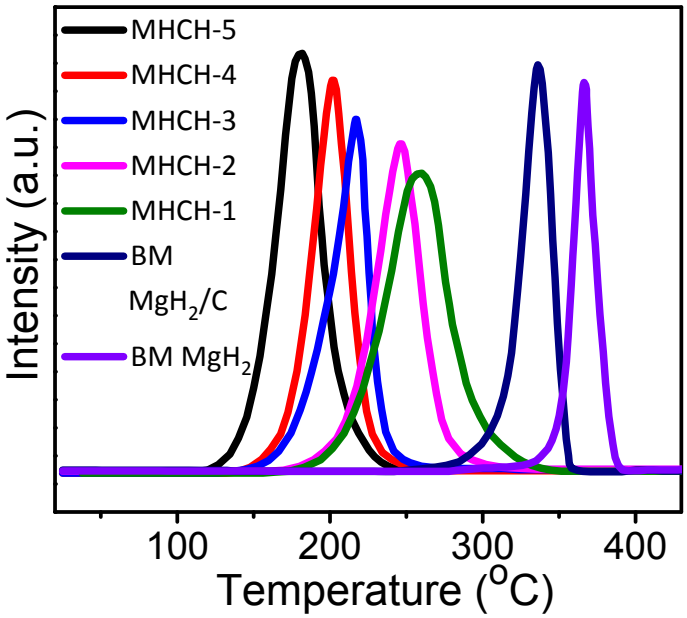

Figure S8. Mass spectra of the ball-milled MgH_2, ball-milled MgH_2/C, and as-synthesized MHCH samples.

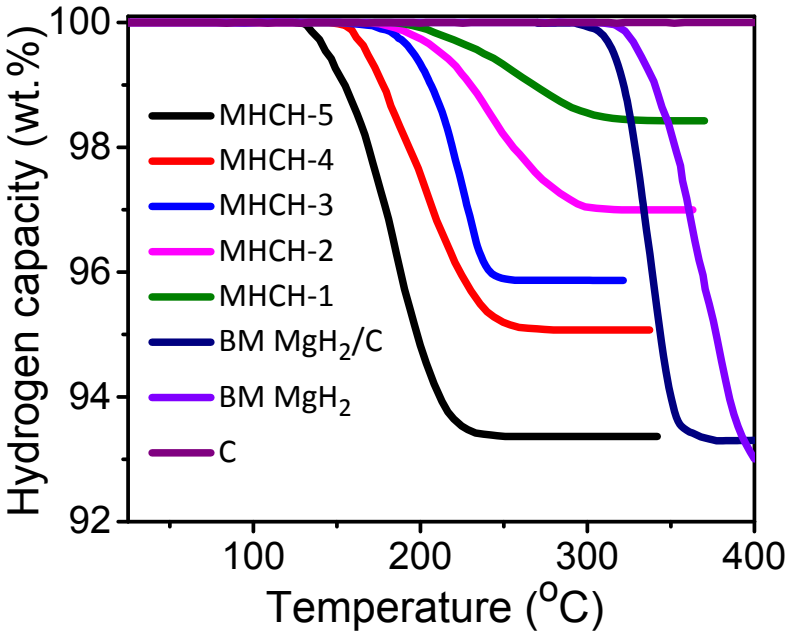

Figure S9. Thermogravimetric analysis (TGA) profiles of carbon, ball-milled MgH_2, ball-milled MgH_2/C, and as-synthesized MHCH samples.

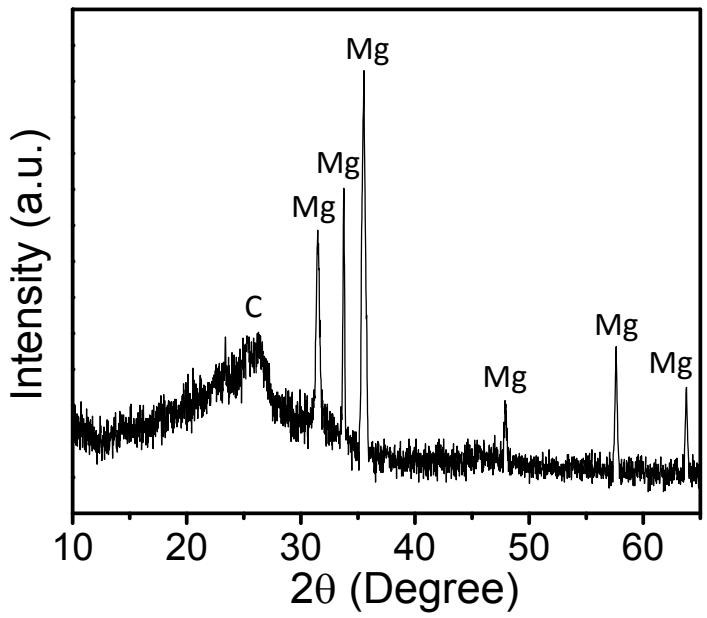

Figure S10. X-ray diffraction pattern of the MHCH-5 after dehydrogenation at 180 ^{o}C.

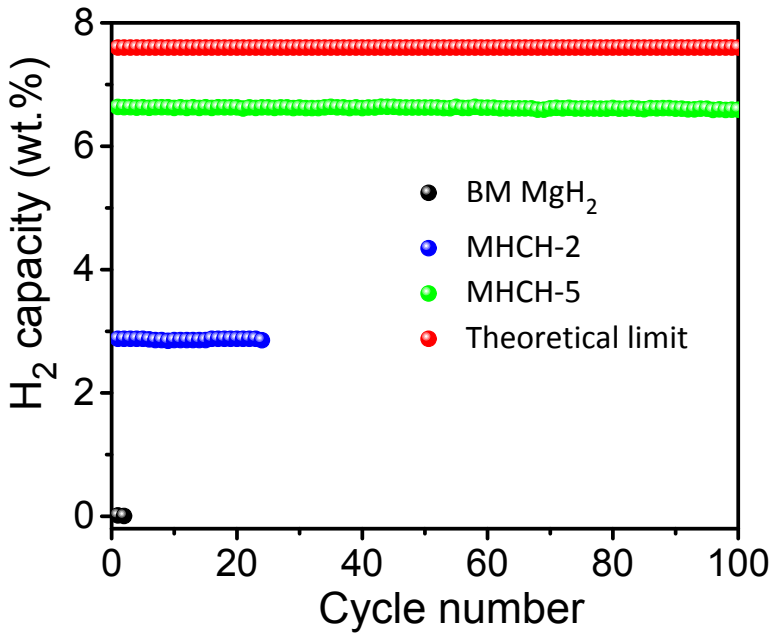

Figure S11. Normalization of the reversible hydrogen storage capacity versus the cycle number of ball-milled MgH_2, MHCH-2, and MHCH-5 samples along with theoretical value of MgH_2.

The hydrogen capacity over 100 cycles for MHCH-5 is much better than MHCH-2 and BM MgH_2 samples. Further, the achieved performance is very high than target of US, Department of Energy (DOE-2020). However, there is large scope to improve hydrogen capacity to reach theoretical limits of MgH_2. In order to enhance the hydrogen capacity further, it needs to improve the structural and electrical properties of prepared catalysts.

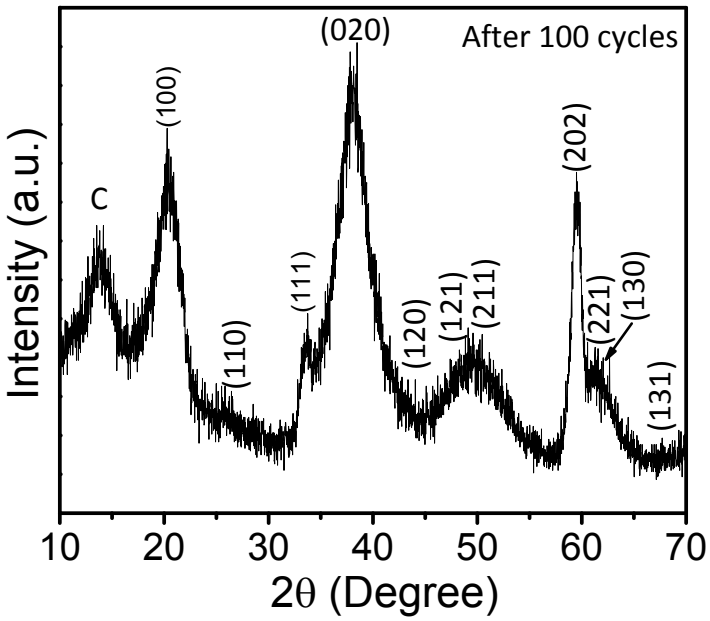

Figure S12. X-ray diffraction pattern of the MHCH-5 over 100 cycles of continuous operation.

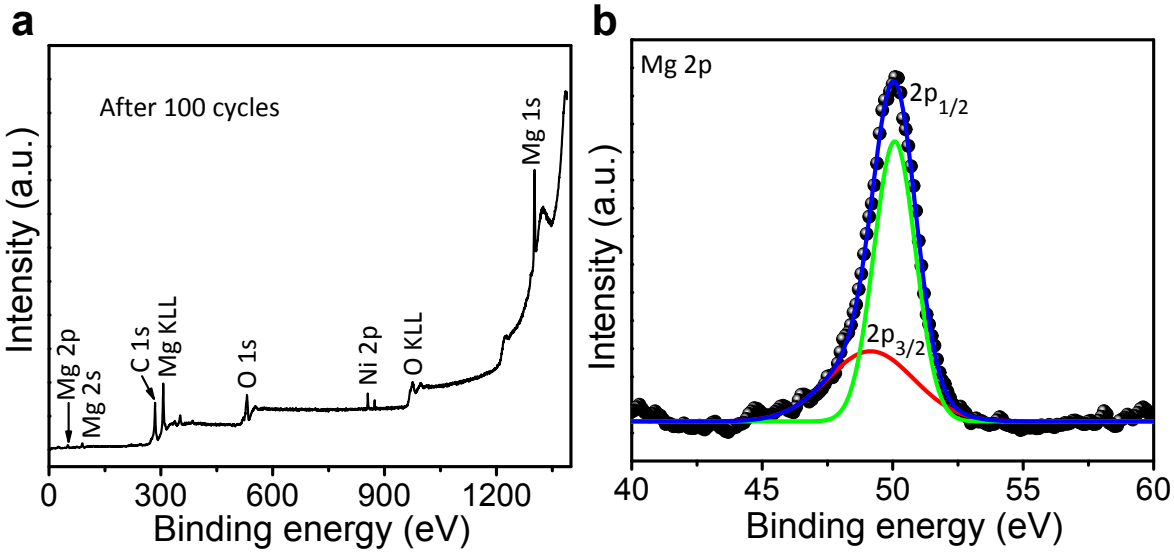

Figure S13. (a) XPS survey spectra and (b) high resolution Mg 2p spectra of the MHCH-5 over 100 cycles of continuous operation.

Typical survey scan spectra clearly shows presence of Mg 2p, Mg 2S, C 1s, Mg KLL, O 1s, Ni 2P, O KLL, and Mg 1s peaks after 100 cycles stability test, confirms that prepared MHCH-5 is highly robust for longer time. We did not observe any loss in elements such as Mg, Ni, C, etc. Further, high resolution Mg 2P spectra also confirms the presence of $2p_{3/2}$ and $2p_{1/2}$ core states at 49.15 and 50.08 eV, illustrating similar nature with as-prepared catalyst.

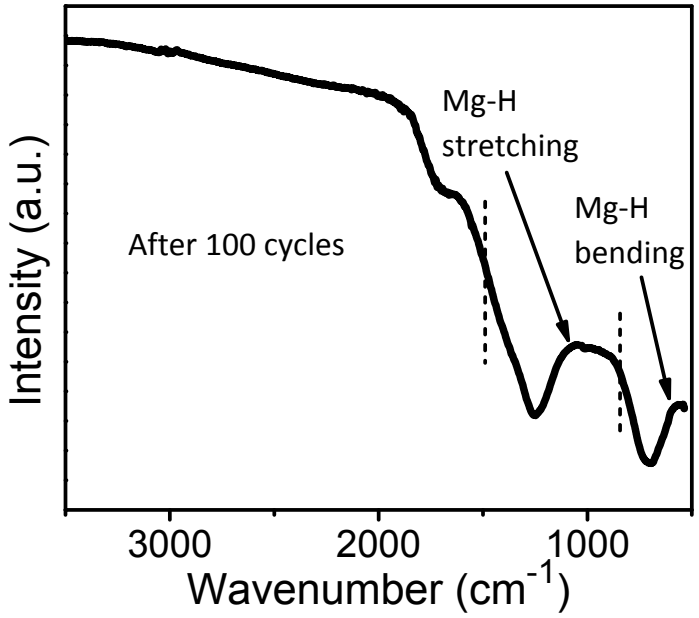

Figure S14. FTIR spectrum of the MHCH-5 over 100 cycles of continuous operation.

No impurity and/or loss were observed by FTIR spectra after the 100th cycles of de-/hydrogenation and well preserved characteristic peaks with absence of any byproducts were obtained in the catalysts, endorsing the high cycling stability of MHCH-5 samples.

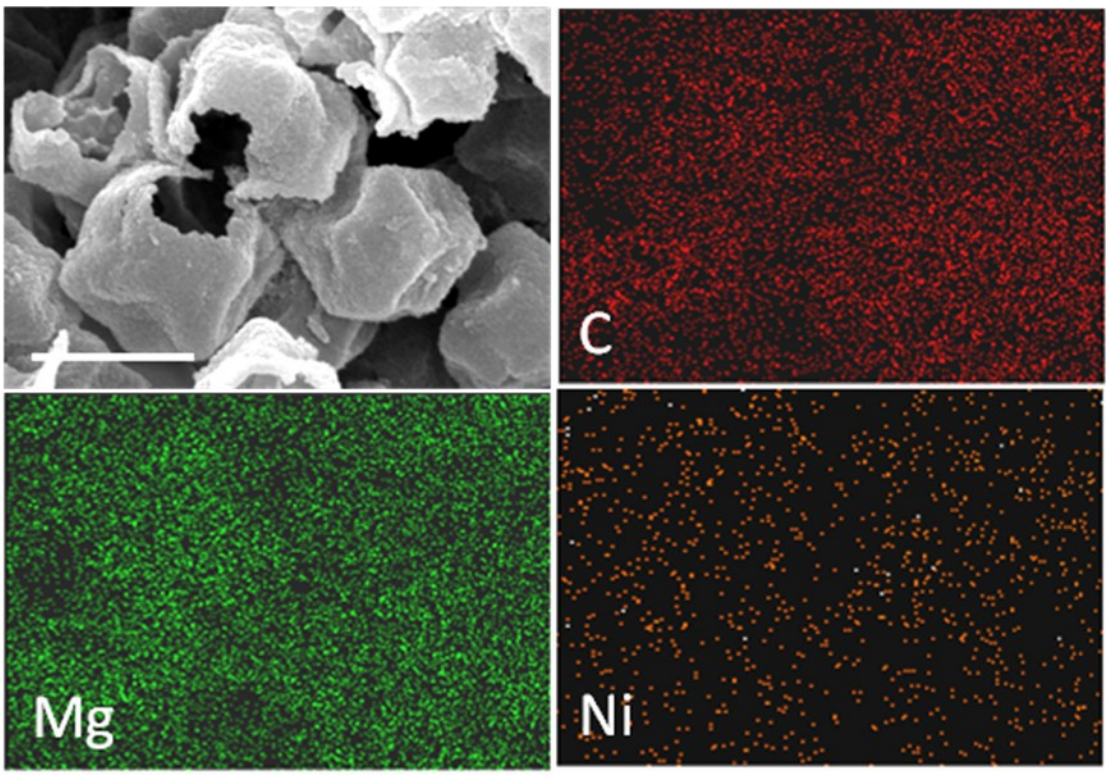

Figure S15. SEM image of MHCH-5 and the corresponding elemental mappings of C, Mg, and Ni after 100 cycles (scale bar =100 nm).

At the end of 100th de-/hydrogenation cycles, we analyzed the morphological changes in the MHCH-5 hybrid and found that the nanostructure at this stage is very similar to that of freshly prepared catalysts, without any emergence of physical damage and noticeable aggregation. Further, the SEM image and corresponding EDS mapping also confirms the existence of C, Mg, and Ni elements with homogeneous distribution over 100 cycles demonstrating long-term stability of prepared catalysts.

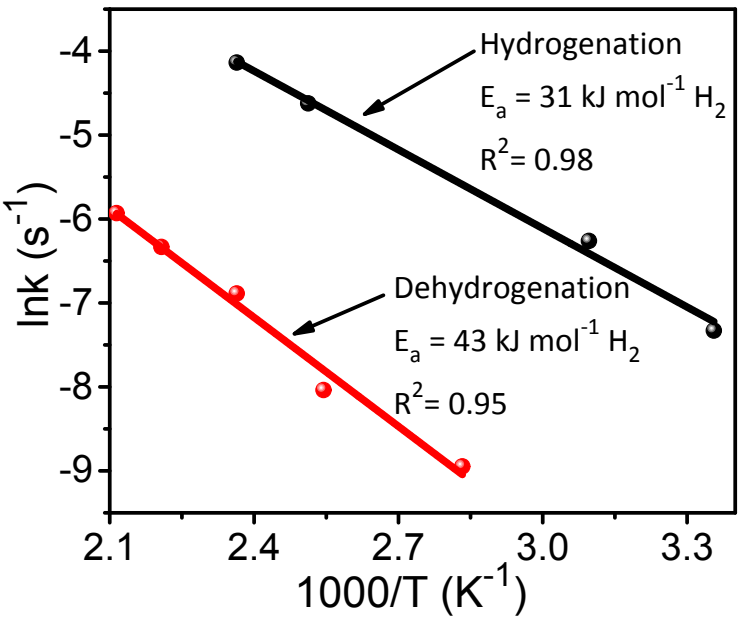

Figure S16. Arrhenius plots of the MHCH-5 for the hydrogenation and dehydrogenation kinetics.

The apparent activation energy was determined from the slope of fitted lines. It is seen that apparent activation energy was substantially lowered because of synthesis of MgH_2 NPs at room temperature with unique 3-D nanostructure of metal incorporated carbon. These results quantitatively evidenced the superior catalytic effects (i.e., obvious enhancement in the hydrogen release kinetics) of MHCH-5 hybrid on the de-/hydrogenation reactions.

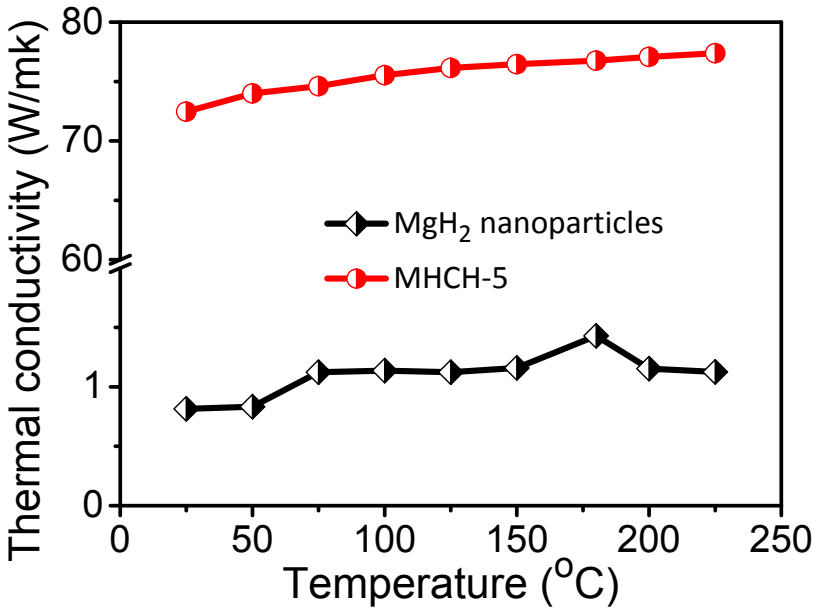

Figure S17. Thermal conductivity of MgH_2 nanoparticles and the as-prepared MHCH-5 samples at different temperatures.

Thermal conductivity of MHCH-5 shows slight increment from 72.46 to 77.38 W/mK with temperature from 25 to 225 °C, whereas MgH_2 NPs shows only 0.82 to 1.12 W/mK. This results show the excellent enhancement in the thermal conductivity for MHCH-5 than MgH_2 NPs with respect to temperature, confirming the outstanding thermal stability of prepared MHCH-5.

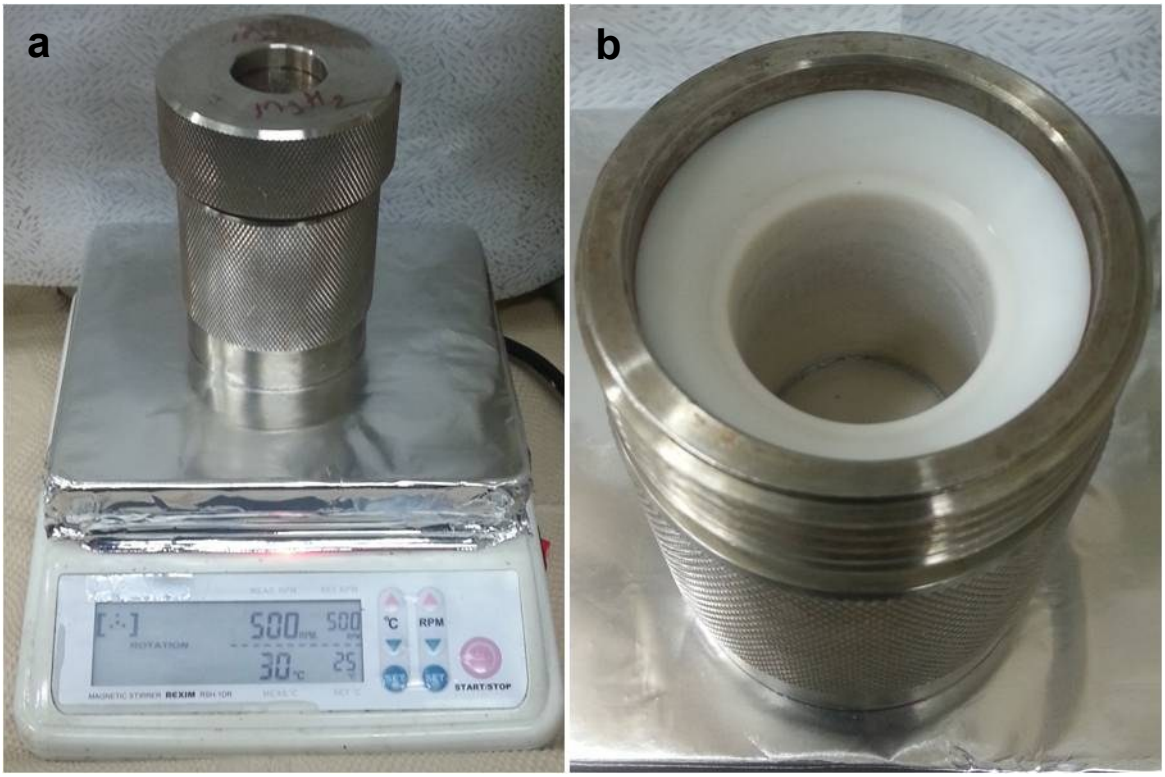

Figure S18. (a, b) Photograph of the experimental reactor utilized for the solvothermal process. The results clearly indicate the fabrication of MgH_2 based nanostructures at room temperature without external hydrogen pressure. Therefore, this experimental system provides breakthrough green technology for hydrogen fuel cell commercialization.

Table S1. Total hydrogen discharge capacities of the MHCH samples evaluated based on the TPD and ^{1}H NMR profiles. The calculation of the capacity utilizes the area under curves obtained from Figure S8 and broad resonance of ^{1}H NMR (Figures 2 a-c, black line). This confirms the approximately similar performance for H_2 capacity by using both analyses.

Catalysts	H_2 capacity from TPD (%)	H_2 capacity from NMR (%)
MHCH-3	68.3	66.12
MHCH-4	63.5	61.8
MHCH-5	78.2	76.02

Table S2. Onset and peak dehydrogenation temperatures and the released practical capacity of hydrogen of the prepared catalysts calculated from TPD analysis.

Catalysts	Onset temperature, T_{onset} (^{o}C)	Peak temperature, T_{peak} (^{o}C)	H_2 capacity (wt.%)
MHCH-5	121	180	6.63
MHCH-4	141	202	4.81
MHCH-3	153	217	4.12
MHCH-2	172	246	2.95
MHCH-1	177	259	1.56
BM-MgH_2/C	274	337	6.5
BM MgH_2	321	366	7.1

Table S3. The hydrogen storage capacities of reported catalysts at room temperature.

Catalysts	Room temperature, H_2 storage capacity (wt.%)	Time (hr)	Reference
MHCH-5	3.86	1	This work
MgH_2 + 5 wt% (Ni-MOF-74)	2.7	10	S8
Ni-MHGH-75	2.3	1	S9
MgH_2 + Ni-VO_x /AC	1.3	6	S10
MgH_2/0.1TiH_2	2.9	4	S11

Table S4. The performances of reported MgH_2-based catalysts. The present MHCH-5 show excellent hydrogen capacity (6.63 wt%) and enthalpy (49.1 KJ mol^{-1}) over the reported literatures at relatively lower de-/hydrogenation temperature (180 ^oC), illustrating uniqueness of the prepared catalyst. Further, we could achieve best loading percentage of MgH_2 NPs over other reported catalysts. This features the prepared MHCH-5 can be readily scalable for practical hydrogen storage devices such as hydrogen storage tanks, hydrogen fuel vehicles etc.

Catalyst	Loading capacity (wt.%)	De-/hydrogenation temperature (^oC)	Enthalpy (KJ mol^{-1})	H_2 capacity (wt. %)	Reference
MHCH-5	60	180	49.1	6.63	This work
MgH_2-Ni-MOF	50	300	-	5.6	S8
Ni-MHGH-75	75	200	62.1	5.4	S9
MgNCs/PMMA	61	200	-	4.6	S12
MgH_2/CA-9	10	300	60	1.7	S13
Mg/CMK20/90	25	250	52.38/71.67	5.1	S14
Mg-In	-	300	70.87	3.2	S15
MgH_2-MOF-177	10.5	200	-	0.8	S16
MgH_2-VTiCr	-	350	76.31	3.1	S17
MgH_2-$Fe_3O_{4@}$GS	40	300	60.62	4.4	S18
Mg_6Pd	18.5	300	63.8	1.4	S19
MgH_2/PMMA	65	300/200	-	4.9	S20
MgH_2-Carbon template	13	250	66.34	1.1	S21
MgH_2/carbon scaffolds	15	252	-	1.3	S22
MgH_2-Carbon aerogel	18	700	-	1.4	S23
$Mg@Ni_8Gn_2$	90	200	74.6	6.28	S24
Mg/C	-	200	63	-	S25

Theoretical Johnson-Mehl-Avrami (JMA) models

$$\left[-\ln(1-\alpha)\right]^{1/n} = kt \quad \text{(S1)}$$

$$\alpha = kt \quad \text{(S2)}$$

$$1-(1-\alpha)^{1/n} = kt \quad \text{(S3)}$$

$$1-\left(\frac{2\alpha}{3}\right)-(1-\alpha)^{2/3} = kt \quad \text{(S4)}$$

These kinetic JMA models decide the growth of MgH_2 on supporting materials (such as 1-D, 2-D, 3-D, chemisorption and core-shell growth).

Supplementary References

[S1] M. Verkuijlen, P. Ngene, D. De Kort, C. Barré, A. Nale, E. Van Eck, P. Van Bentum, P. De Jongh, A. Kentgens, *J. Phys. Chem. C,* **2012,** 116, 22169–22178.

[S2] E. Setijadi, C. Boyerb, K. Aguey-Zinsou, *Phys. Chem. Chem. Phys.,* **2012,** 14, 11386–11397.

[S3] S. Singh, A. Singh, K. Aranishi, Q. Xu, *J. Am. Chem. Soc.* **2011,** *133,* 19638–19641.

[S4] S. Yang, K. Chang , H. Tien , Y. Lee , S. Li , Y. Wang, J. Wang, C. Ma, C. Hu, *J. Mater. Chem.* **2011,** *21,* 2374-2380.

[S5] X. Wang, L. Andrews, *J. Phys. Chem. A* **2004,** *108,* 11511-11520.

[S6] X. Xiao, Z. Liu, S. Saremi-Yarahmadi, D. Gregory, *Phys. Chem. Chem. Phys.* **2016,** *18,* 10492-10498.

[S7] S. Xie, X. Han, Q. Kuang, Y. Zhao, Z. Xie, L. Zheng, *J. Mater. Chem.,* **2011,** 21, 7263-7268.

[S8] Y. Jia, C. Sun, Y. Peng, W. Fang, X. Yan, D. Yang, J. Zou, S. Mao, X. Yao, *J. Mater. Chem. A* **2015,** *3,* 8294–8299.

[S9] G. Xia, Y. Tan, X. Chen, D. Sun, Z. Guo, H. Liu, L. Ouyang, M. Zhu, X. Yu, *Adv. Mater.* **2015,** *27,* 5981–5988.

[S10] Y. Jia, L. Cheng, N. Pan, J. Zou, G. Lu, X. Yao, *Adv. Energy Mater.* **2011,** *1,* 387–393.

[S11] J. Lu, Y. J. Choi, Z. Z. Fang, H. Y. Sohn, E. Ronnebro, *J. Am. Chem. Soc.* **2010,** *132,* 6616-6617.

[S12] K. Jeon, H. Moon, A. Ruminski, B. Jiang, C. Kisielowski, R. Bardhan, J. Urban, Nat. Mater. 2011, 10, 286-290.

[S13] Y.Au, M. Obbink, S. Srinivasan, P. Magusin, K.de Jong, P.de Jongh, *Adv. Funct. Mater.* **2014,** *24,* 3604–3611.

[S14] M. Konarova, A. Tanksale, J. Beltramini, G. Lu, *Nano Energy* **2013,** *2,* 98-104.

[S15] C. Zhou, Z. Fang, J. Lu, X. Zhang, *J. Am. Chem. Soc.* **2013,** *135,* 10982−10985.

[S16] D. Lim, J. W. Yoon, K. Y. Ryu, M. P. Suh, *Angew. Chem., Int. Ed.* **2012,** *51,* 9814-9817.

[S17] C. Zhou, Z. Fang, R. Bowman, Jr., *J. Phys. Chem. C* **2015,** *119,* 22261−22271.

[S18] A. Bhatnagar, S. Pandey, A. Vishwakarma, S. Singh, V. Shukla, P. Soni, M. Shaz, O. N. Srivastava, *J. Mater. Chem. A* **2016,** *4,* 14761–14772.

[S19] M. Ponthieu, Y. S. Au, K. Provost, C. Zlotea, E. Leroy, J. F. Fernandez, M. Latroche, P. E. de Jongh, F. Cuevas, *J. Mater. Chem.* A **2014,** *2,* 18444-18453.

[S20] A. Ruminski, R. Bardhan, A. Brand, S. Aloni, J. Urban. *Energy Environ. Sci.* **2013,** *6,* 3267-3271.

[S21] C. Zlotea, F. Cuevas, J. Andrieux, C. M. Ghimbeu, E. Leroy, E. Léonel, S. Sengmany, C. Vix-Guterl, R. Gadiou, T. Martens, M. Latroche. *Nano Energy* **2013,** *2,* 12-20.

[S22] S. Zhang, A. Gross, S. Van Atta, M. Lopez, P. Liu, C. Ahn, J. Vajo, C. Jensen, *Nanotechnol.* **2009,** *20,* 204027.

[S23] T. Nielsen, K. Manickam, M. Hirscher, F. Besenbacher, T. Jensen, *ACS Nano* **2009,** *3,* 3521-3528.

[S24] J. Zhang, Y. Zhu, X. Zang, Q. Huan, W. Su, D. Zhu, L. Li, *J. Mater. Chem. A* **2016,** *4,* 2560.

[S25] P. de Jongh, R. Wagemans, T. Eggenhuisen, B. Dauvillier, P. Radstake, J. Meeldijk, J. Geus, K. de Jong, *Chem. Mater.* **2007,** *19,* 6052–6057